Extreme Size and Irradiance Dependence in High-Resolution Vat Photopolymerization of Hydrogels

Rion J. Wendland*, Orion L. Kafka, Thomas J. Kolibaba, Callie I. Higgins, Grant Draper, Nick Clinton, Raghuveer Lalitha Sridhar, Kalyan Vydiam, Daniel Backman, Aman Kaur, Matt Gelber, Matthew Bedell, Scott Turner, Jason P. Killgore*

R.J. Wendland, O.L. Kafka, T.J. Kolibaba, C.I. Higgins, J.P. Killgore: Applied Chemicals and Materials Division - National Institute of Standards & Technology, Boulder, CO USA

G. Draper, N. Clinton, M. Gelber, S. Turner: 3D Systems, San Diego, CA USA

R.L. Sridhar, K. Vydiam, D. Backman, A. Kaur, M. Bedell: United Therapeutics, Manchester, NH USA

*Corresponding authors: rion.wendland@nist.gov, jason.killgore@nist.gov

Keywords

Vat photopolymerization, working curve, hydrogels, optical coherence tomography, bioprinting, dead zone, oxygen inhibition, cure depth

Abstract

Vat photopolymerization is a high-resolution and high-throughput technology used in many biomedical applications. However, achieving geometric precision in printed devices with features spanning orders of magnitude in length scale is non-trivial. Here, a new characterization tool combining fast, high-resolution optical coherence tomography imaging with a high-powered digital light processing projector enables real time measurements of photopolymer curing. The direct, quantitative measurement of hydrogel working curves (the relationship between cure depth and light exposure) shows that the critical energy for gelation (E_c) exhibits extreme size dependence, demanding a rethinking of gray-scaling light intensity for achieving predictable voxel formation at high resolutions. This *in situ* method also enables measurement of size-dependent working curves and dead zone thicknesses using oxygen permeable window materials, which is impossible via *ex situ* methods. Generally, size sensitivity is amplified at low irradiance, high dye-loading, and in the presence of oxygen permeable windows. Despite the extreme size sensitivity, calibrating the light exposure to the size dependent E_c allows a 3x improvement in layer-growth uniformity compared to a naïve approach. Overall, these results highlight the challenges in high-resolution printing of hydrogels and provide a framework to measure and account for size dependence.

1. Introduction

Bioprinting is at the forefront of medical research, enabling breakthroughs in tissue engineering, regenerative medicine, and pharmaceutical screening.[1–3] Many of the advantages enabled by bioprinting address the fabrication of tissue-like 3D structures, which more closely mimic the human body than traditional 2D cell cultures on plastic materials.[4–6] One of the ultimate goals of bioprinting remains the manufacturing of functional human organs, which would significantly improve health outcomes and end the reliance on donor organs. An important aspect of these functional organ systems is the size scale and resolution needed to mimic the inherent complex geometries displayed by these systems. For example, blood (arteries to capillaries) and air (trachea to bronchioles) pathways can range from micrometers to centimeters in thickness and diameter.[7,8] While the highest resolutions in additive manufacturing have been achieved with two-photon polymerization, the serial nature of the method typically limits total part size. Given the requirement to print relatively large scaffolds and organs while retaining micron-scale fidelity, vat photopolymerization with digital light processing (DLP) or liquid crystal display (LCD) technologies is a promising fabrication technique for bioprinting. By individually addressing the pixels in the light engine, tens of millions of simultaneous reactions can be controlled in a single layer. The size of the projection dictates the maximum lateral part dimensions, while the pixel size and pitch dictate theoretical resolution. Despite high theoretical hardware resolution (e.g., single micrometer projector resolution is commercially available), realizing that resolution in a complex 3D bioprint demands optimization of material and process.

In vat photopolymerization of plastic resins, numerous studies have highlighted the dependence of voxel formation kinetics on programmed feature size (i.e. the size of the feature in the digital mask). Repeatedly, smaller features have been shown to cure slower than larger features.[9–13] Thus, the exposures that precisely produce small features will overcure large features. The size dependence has been attributed to both light engine and resin characteristics. For the light engine, pixels may be considered as individual gaussian emitters with spatially varying intensity. When pixels are combined in a larger area, the tail from one gaussian adds to the peaks of neighboring pixels, producing a higher effective irradiance.[10] For the resin, size dependence could arise from increased diffusion of species into or out of the voxel, resulting in alteration of the polymerization reaction.[12,14] Additionally, studies in plastic resins have highlighted differences in curing kinetics based on light irradiance levels.[14–19] This phenomenon has been attributed to different rates of radical generation for different irradiances. Higher irradiances increase the rate of radical generation, which can increase the likelihood of radical terminations and decrease the ratio of propagation to termination rate.[19–22] Previous studies have adjusted radiant exposure to account for light scattering effects (specifically with cell-laden resins) on printed resolution and fidelity of hydrogels.[23,24] Here, we extend that approach to consider size- and irradiance-dependent effects that must be considered in higher resolution printing of hydrogel materials.

To date, size- and irradiance-dependence in plastic resins has largely been studied *ex situ*, using plan view optical microscopy and measurement of cure depth C_d. Typical optical microscopy measurements have considered the lateral dimensions of a features in a single

printed layer relative to the dimensions programmed in the photomask.[25,26] Cure depth measurements have revealed size dependence by comparing feature thickness for the same exposure, at different lateral feature size. The exposures can be cured into a comparatively deep pool of resin, resulting in unbounded vertical growth of the layer. For cure depth measurements, the thickness (and often sidewall profile) of a single layer printed feature is often determined via micrometer, stylus profilometer, optical profilometer, or oblique microscopy.[9,20,27] The resultant cure depth data can be considered directly, or interpreted via the Jacob's working curve:

$$C_\mathrm{d} = D_\mathrm{p} \ln\left(\frac{E_0}{E_\mathrm{c}}\right) \tag{1}$$

where, D_p is the depth of light penetration corresponding to $1/e$ light absorption, E_0 is the incident radiant exposure used to cure the measured feature, and E_c is the critical exposure required to achieve gelation at zero cure depth.[28] For working curve measurements, the C_d measurements are made at a range of discrete E_0 such that D_p and E_c can be determined by the slope and intercept of the semi-log plot, respectively. To date, E_c has been strongly revealing of size dependence in plastics, while D_p shows more modest dependence.

Though refinement of this method can produce highly reproducible data, it can be time and resource intensive. As such, recent efforts have been made to study photopolymerization reactions *in situ*.[14,29–32] These real-time microscopy-based measurements have the potential to be higher throughput, while also being capable of observing transient phenomena that are missed during the interval from processing to characterization. While previously studied in plastic resins, optical microscopy techniques are uniquely suited for hydrogel resins, as we recently demonstrated by exploring bulk hydrogel working curve measurements.[33] Contact methods (such as micrometers) can impart significant deformation and be prone to moisture dependent properties if performed *ex situ*, resulting in inaccurate working curves compared to non-contact, optical methods. Given the challenges and unknown size-effects associated with high-resolution hydrogel bioprinting, we introduce an *in situ* microscopy technique using optical coherence tomography (OCT) to measure size- and irradiance-dependence of hydrogels in a high-throughput, high-resolution, and real-time manner. OCT is a noninvasive imaging technology that uses galvo-scanning near-infrared low-coherence interferometry to detect optical interfaces throughout a structure. In photopolymer and bioprinting applications, OCT has previously been used to measure *ex situ* cure depths of plastic and hydrogel resins,[33,34] characterize surface roughness of dental prosthetics,[35] perform 3D analysis of extrusion printed contructs,[36,37] and visualize resin flow rate in injection continuous liquid interface printing.[38,39]

In this study, we develop a hybrid instrument combining a 5.4 μm resolution, high power projector with a custom sample stage and OCT imaging system to enable real time visualization of voxel gelation in hydrogels. To enable visualization with OCT, we designed a hydrogel resin that scatters significantly more infrared light upon gelation compared to unpolymerized material. As such, feature cure depths versus radiant exposure (i.e., the working curve) can be measured in a high-throughput, accurate manner (**Figure 1**). Using this system, we compare *in situ* hydrogel working curves (and the subsequent Jacobs fit parameters) as a function of lateral boundary conditions (feature width w_f and feature spacing s_f) and light irradiance. We then investigate the

size dependencies under print relevant conditions including resin formulation (dye loading) and window material (oxygen permeable versus non-permeable). Lastly, we demonstrate that calibrating the light exposure to the size dependent E_c in a single- and multi-layer printed part significantly improves the cure depth uniformity compared to a naïve, single exposure approach. Overall, these results demonstrate the capabilities of *in situ* photopolymerization measurements and establish the size dependencies of hydrogel materials, helping to overcome the challenges of high-resolution bioprinting.

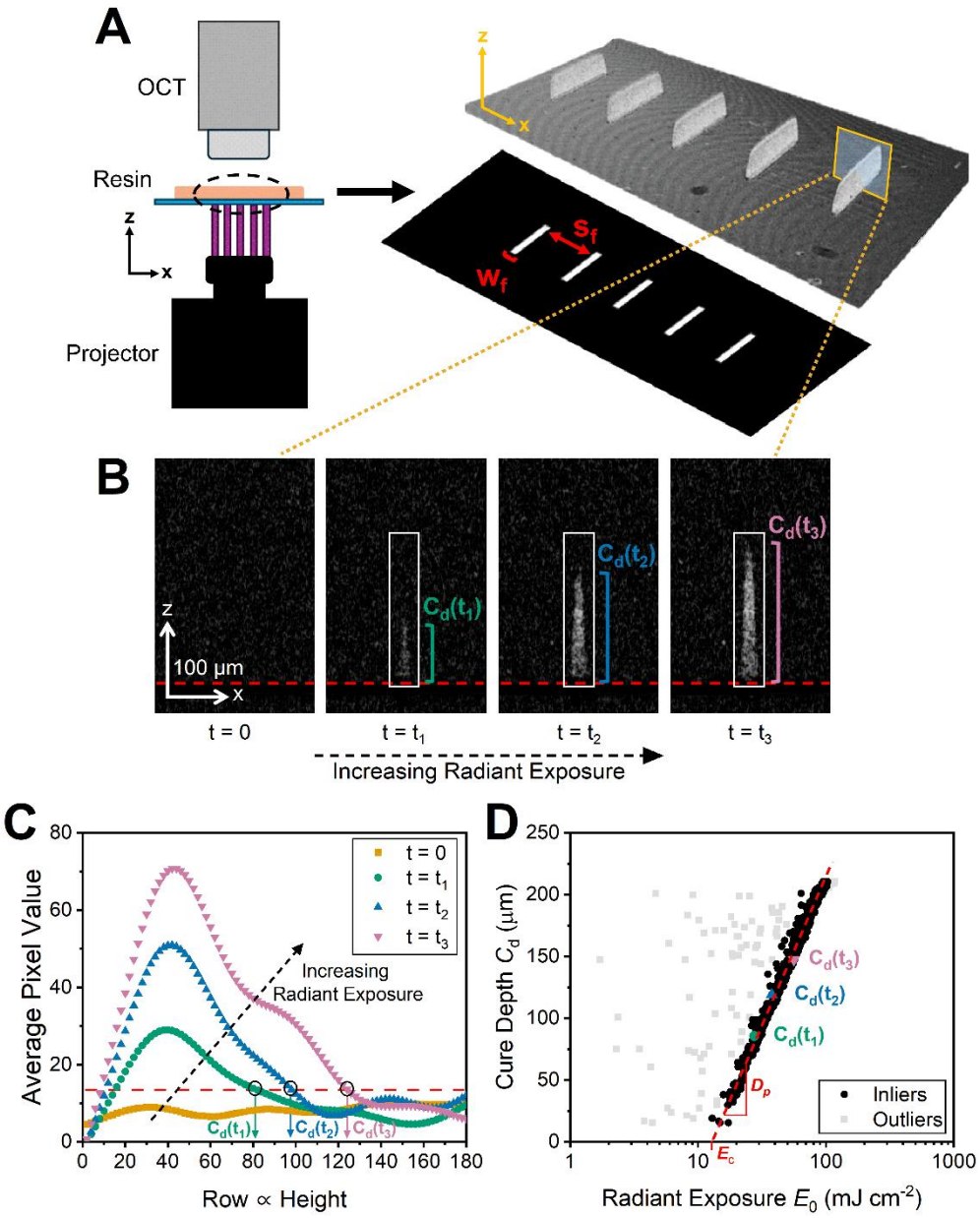

Figure 1. OCT enables *in situ* measurements of photopolymer features. **A**) Schematic of experimental setup detailing an example photomask with feature width w_f and spacing s_f, along with 3D OCT image of the polymerized features. **B**) An XZ projection imaged through time is used to determine feature height. Red dashed line indicates the resin-window interface. White boxes indicate the bounding box around the feature while brackets indicate feature cure depth at a given time. Scale bars in z- and x-directions represent 100 μm. **C**) Representative calculation of feature height using the average pixel value in each row of a bounding box around a feature. Red line represents the baseline threshold value (e.g., noise floor). For a given time, the last row value that is above the baseline threshold indicates the feature height (arrows). **D**) Representative working curve data with log-linear fit (red line) of the Jacobs equation, giving parameters D_p (slope) and E_c (x-intercept). Colored data points correspond to the timing snapshots of the representative data in (**B**) and (**C**). Random sampling consensus regression was used to determine inlier and outlier data.

2. Results and Discussion

Hydrogel Working Curves are Dependent on Incident Irradiance and Feature Width

To evaluate the size dependent curing properties of hydrogels, we used *in situ* OCT imaging to measure cure depth versus radiant exposure (i.e., the working curve) at various feature widths w_f and irradiance levels I_0 (**Figure 2A-C, Figure S1-4**). To reduce the findings to a smaller number of parameters, we used the Jacobs model to fit the subsequent working curve data and extract parameters D_p (light penetration depth) and E_c (critical exposure energy). D_p did not exhibit a significant size dependent relationship, although a slight trend of decreasing D_p with decreasing w_f was observed. D_p did show a strong positive correlation with irradiance, with the value increasing roughly 50 % as I_0 increased from 5.7 mW cm^{-2} to 446 mW cm^{-2} (**Figure 2D**, **Table S1**). Correspondingly, E_c exhibited significant dependence on feature width and irradiance. At low irradiances, decreased w_f resulted in dramatically increased E_c. This dependence appeared to follow an exponential decaying relationship, with E_c values at the large feature plateau approaching 13 mJ cm^{-2} and 11 mJ cm^{-2} for I_0 = 23 mW cm^{-2} and I_0 = 5.7 mW cm^{-2}, respectively. Notably, for I_0 = 5.7 mW cm^{-2}, the smallest features did not polymerize within the experimental time, resulting in E_c greater than 300 mJ cm^{-2} which may approach a practical infinity (not polymerizable) given the measured trends. Significant size dependence was not observed for higher irradiances (223 mW cm^{-2} and 446 mW cm^{-2}). However, as irradiance increased, plateau E_c also increased from 11 mJ cm^{-2} to 40 mJ cm^{-2} (**Figure 2E**, **Table S1**).

Overall, *in situ* OCT experiments confirm hydrogel working curves are dependent on both incident irradiance and lateral feature size, with the most significant changes in E_c seen at low irradiances and small feature widths. Working curve dependence on irradiance has been previously observed in plastic photopolymer systems. Here, the trend of increasing E_c with increasing irradiance agrees with previous studies.[16,17,19] Higher irradiance linearly increases the rate of radical generation, increasing the chance of radical termination by recombination (the rate of which scales with the square of radical concentration) and increasing E_c. Additionally, increasing E_c with decreasing feature size has been previously observed in plastic photopolymer systems.[10–12] Though light engine design and material transport properties have both been

suggested to explain size dependent properties, we postulate that diffusion dominates the observed responses in our low-solids hydrogels. If pixel overlap was the primary cause, size dependent effects should be uniform across all irradiances. Instead, size dependencies are amplified at lower irradiances, where reaction durations are extended.

To elucidate the diffusing species responsible for size dependence, we compared the characteristic diffusion time constants $\tau(w_f)$ for oxygen in water and PEGDA in water using a simplified 1D model (**Figure 2F**). We used O_2 and PEGDA's diffusivity in water as an upper bound and estimated a reduced diffusivity for a lower bound based on decreased diffusion across polymerized hydrogels.[40–43] We focus on these two species as O_2 strongly inhibits the acrylate reaction and local depletion is required prior to polymerization,[44–46] and the fact that PEGDA oligomers could diffuse out of the reaction volume prior to incorporation into the network. The choice of a 1D model was justified considering that maximal oxygen depletion, and thus minimum $\tau(w_f)$, occur at the window interface at the time of initial gelation. The value of $\tau(w_f)$ is defined by

$$\tau(w_f) = \frac{\left(\frac{w_f}{2}\right)^2}{D}, \tag{2}$$

where D is the diffusivity coefficient and $w_f/2$ is the characteristic length representing the edge to center distance of the reaction volume. The measured time to gelation $t_c = E_c / I_0$ at multiple irradiances versus w_f is also plotted. By examining the feature width where $t_c(w_f)$ strongly departs its plateau value, compared to the characteristic diffusion time for the species considered, insight into the root cause can be obtained. At I_0 = 5.7 mW cm^{-2}, size dependence becomes evident at $w_f \approx 100$ µm, coincident with the characteristic diffusion time of ≈1 s for O_2 to diffuse 100 µm bidirectionally. If diffusion of PEGDA were dominating, size dependence would not be expected to occur until features were smaller than 40 µm. Likewise, at I_0 = 23 mW cm^{-2} the inflection from the t_c = 0.5 s plateau occurs at $w_f \approx 60$ µm, close to the characteristic diffusion time of $\tau \approx 0.4$ s for O_2 to diffusion. At the higher irradiances of 223 mW cm^{-2} and 446 mW cm^{-2}, critical times for gelation are ≈100 ms, and the effects of O_2 diffusion only just start to become apparent at less the 20 µm feature size. It should be noted that these calculations focus only on lateral diffusion, and diffusion of species in the z-direction may also play a role. Generally, when feature width of the projected light is decreased, there is a shorter time required for oxygen to diffuse into the projected light area (based on shorter widths from the lateral boundaries to the center of the feature). Thus, there is a greater inhibition time as feature width decreases, observed here as an increase in E_c. When considering the combined size and irradiance dependence, it is important to recognize that these observations hold at the instant of gelation, when $C_d = 0$. As the voxel grows vertically, irradiance reduces due to light absorption, and size dependence could appear later in the voxel formation, even if it was absent at the window. While purging the sample with an inert gas such as nitrogen or argon could help confirm these oxygen inhibition predictions, the OCT-projector system is currently not set up for such experiments. We also point out that although size dependence was most dramatic at lower irradiances and largely disappeared at higher irradiances, our lowest irradiance is higher than observed on many LCD-

based printers, and our second lowest irradiance is representative of typical DLP printers; without greater access to higher powered printers, these effects cannot be ignored.

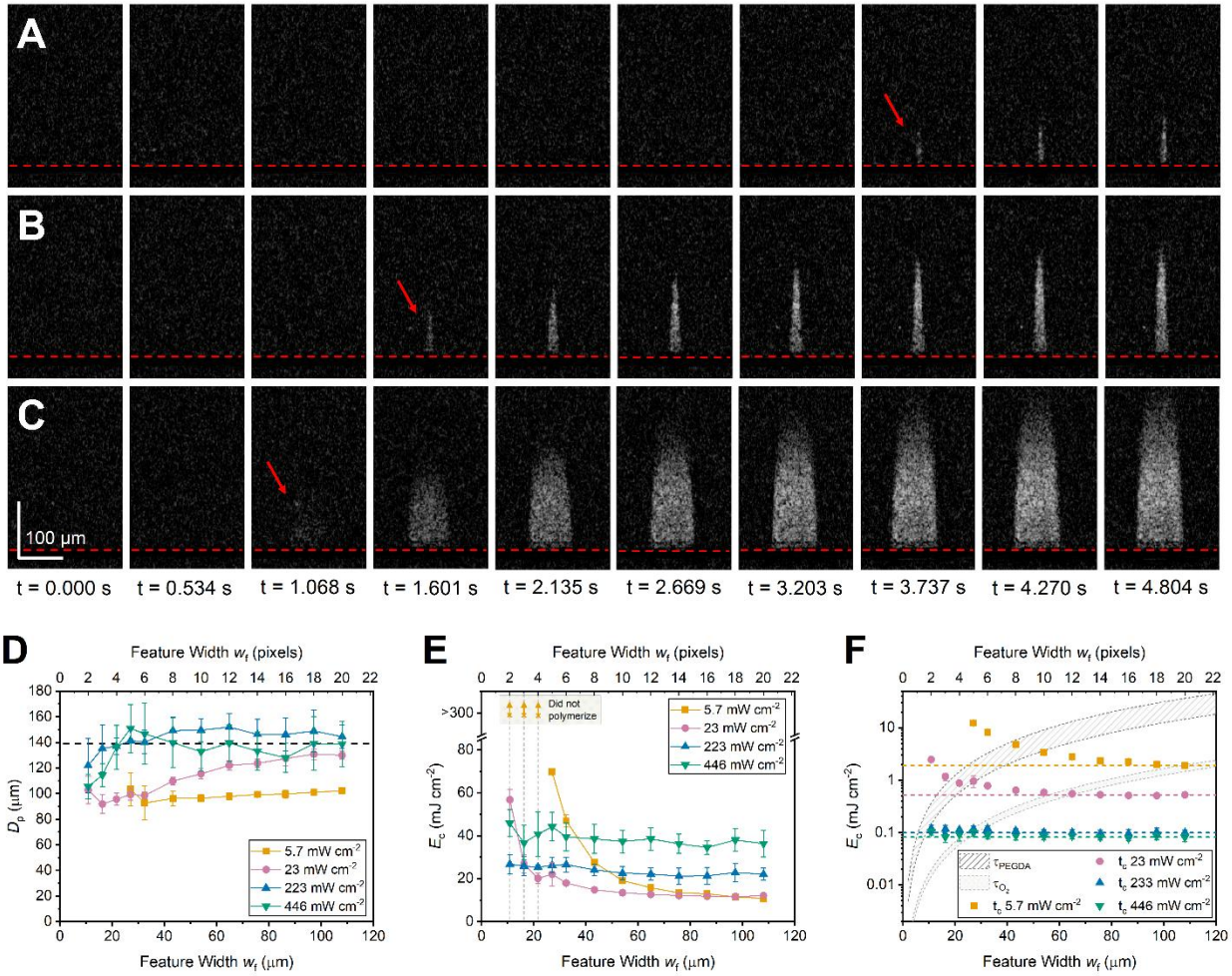

Figure 2. Hydrogel photopolymer working cures exhibit size dependent properties, with significant impacts to E_c as feature width decreases. Representative image sequences of (**A**) 10.8 µm, (**B**) 27 µm, and (**C**) and 108 µm wide features at irradiance I_0 = 23 mW cm^{-2}. Red dashed lines indicate resin-window interface, scale bars represent 100 µm. **D**) D_p versus feature width for four different irradiances. Dashed line indicates optical D_p measured using UV/Vis. **E**) Corresponding E_c versus feature width for the tested irradiances. Arrows represent conditions that did not polymerize during the experimental observation, resulting in E_c greater than 300 mJ cm^{-2}. **F**) One-dimensional diffusion model compares the characteristic time constants τ of oxygen and PEGDA (shaded regions) to the critical exposure cure time (t_c) for each irradiance. Dashed lines indicate the plateau t_c for each irradiance. Data represent mean ± standard deviation of at least six replicates. All data points for D_p and E_c are shown in **Figure S5**.

Lateral Feature Spacing Influences E_c and Pattern Fidelity

In addition to investigating how feature size influences the working curve and polymerization kinetics, we also investigated the influence of feature spacing at an irradiance of

23 mW cm^{-2}. Here, the photomask patterns had one of two possible widths (w_f = 10.8 μm or w_f = 108 μm) with edge-to-edge feature spacing s_f ranging from 5.4 μm to 270 μm (**Figure 3A-C**). Importantly, E_c decreased with decreasing s_f for both small and large w_f. At large s_f, a plateau E_c consistent with each feature width is observed. As the s_f decreases, E_c also decreases, with 10.8 μm features showing a 4-fold reduction in E_c (roughly 60 mJ cm^{-2} to 15 mJ cm^{-2}). Larger, 108 μm features were less affected by s_f, with E_c decreasing from roughly 15 mJ cm^{-2} to 10 mJ cm^{-2} (**Figure 3D**, **Table S2**). As s_f decreased, smaller features appeared to behave more like large features, with boundaries between features becoming less distinct (i.e. lateral overpolymerization). In small w_f features, E_c differences were also observed between interior features (bounded on both sides by other features) and exterior features (only bounded on one side). Exterior features, while still influenced by decreased s_f, had higher E_c across all spacings, indicating less dependence on neighboring features (**Figure 3D**, **Table S2**).

The photopolymerization impacts of closely patterned features (termed the "proximity effect") has been studied in high resolution, 3D printing, typically micro vat photopolymerization and two-photon polymerization systems.[47–49] Both light bleeding from neighboring pixels and oxygen diffusion have been shown to influence achievable feature resolution. While the results from these experiments do not clearly differentiate between the two causes, they highlight the importance of spatial interactions in hydrogel printing. Importantly, the width of neighboring features also impacts the curing reaction and working curve parameters. Decreasing s_f with alternating 10.8 μm and 108 μm features resulted in a different response than when the feature widths were matched (**Figure S6**). Compared to the previous matched patterns, E_c of the 10.8 μm features in alternating patterns did not reach the plateau E_c until larger spacings (roughly 150 μm versus 75 μm). These plateau values in s_f for both matched and alternating features are appreciably larger than the plateau values observed in w_f, suggesting that adjacent depletion of oxygen is a major consideration when engineering uniform voxel growth. Notably, for the alternating small-large patterns, the large features gel sooner than the small features. Sequential illumination of different features or optimization of projected light duty cycles in a layer may provide a pathway to predictive voxel growth in masks with varying feature sizes and close spacing.[50,51] These s_f studies provide guidance on the length scales over which masks could be partitioned in sequential illumination.

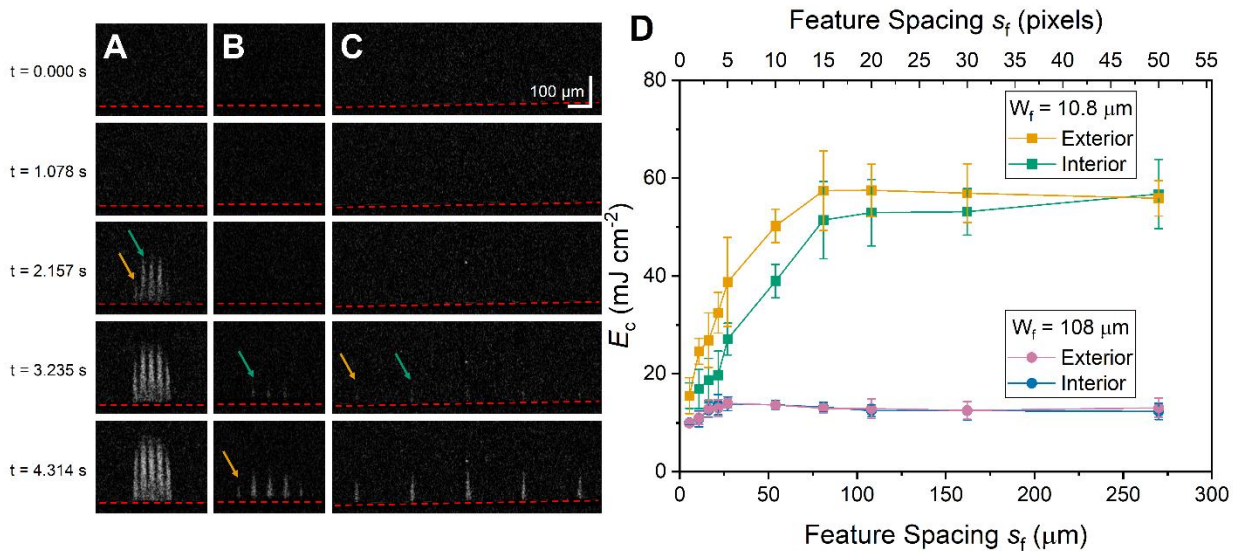

Figure 3. Feature spacing significantly impacts E_c at low irradiances. Representative image sequences of 10.8 µm features spaced (**A**) s_f = 16.2 µm, (**B**) s_f = 54 µm, and (**C**) s_f = 162 µm apart. Red dashed lines indicate resin-window interface, scale bars represent 100 µm. Colored arrows indicate Interior and Exterior features, which correspond to the subsequent graph. **D**) E_c of Interior and Exterior 10.8 µm and 108 µm features at various feature spacings. Data represent mean ± standard deviation of at least four replicates.

Oxygen Inhibition Dead Zone is Dependent on Feature Width

3D printer window material is typically chosen to decrease surface adhesion between the previous printed layer and the window. This design is especially relevant for hydrogel materials, which have a significantly lower strength than plastic polymers and can be prone to failure if the adhesive force between layers is less than the adhesive force to the window. Some window materials rely on low surface energies, while others are oxygen permeable and leverage the resulting oxygen inhibition dead zone to significantly reduce adhesion forces.[52,53] Here, we compared the size dependencies of working curves for three commonly used window materials (PDMS 10:1, AF 2400, and nFEP-PFA) at a constant irradiance of 23 mW cm^{-2}. Of the materials tested, PDMS and AF 2400 are known to be oxygen permeable, which results in an oxygen inhibition zone clearly observed using real time OCT (**Figure 4A-B**). On the other hand, Glass and nFEP-PFA did not have a measurable dead zone, (**Figure S7**, **Table S3**). Interestingly, for PDMS and AF 2400, the depth of the dead zone is dependent on feature size: as the w_f decreases, the oxygen dead zone depth increases (**Figure 4C**). This has significant impact on high resolution printing wherein an assumed layer thickness may be entirely dead zone for small features, even though large, easily observed features appear. When comparing the Jacobs fit parameters to working curves between window materials, D_p was relatively unchanged, with all groups showing a trend of decreasing D_p with decreasing w_f (**Figure 4D**, **Table S4**). However, at small w_f, window material was significant in terms of E_c. Compared to the Glass control, PDMS, AF2400, and nFEP-PFA exhibited increased E_c at small w_f (< 30 µm). Notably, the smallest

feature width (10.8 μm) was unable to polymerize on PDMS, AF 2400, or nFEP-PFA during the experimental time, resulting in a hypothetical E_c greater than 300 mJ cm^{-2} (**Figure 4E**, **Table S4**). On the oxygen permeable materials PDMS and AF 2400, the 16.2 μm feature was also unable to polymerize during the experimental time. Overall, the presence of an additional oxygen-rich boundary increases the size dependency of E_c, with smaller feature widths seeing a greater increase in E_c for oxygen permeable materials (PDMS and AF 2400). However, at large feature sizes, working curve parameters were consistent across all materials. For larger feature sizes, *ex situ* working curve measurements on glass substrates would be predictive of those observed on a printer, given equivalent light sources. It should be noted that consistent with the methodology described previously and to ensure reliable comparisons, cure depth is measured as the distance from the resin-window interface to the top of the sample, even for conditions that displayed an oxygen inhibition "dead zone". This results in a similar extrapolated E_c for oxygen permeable and non-permeable windows, however, the radiant exposure necessary for the first signs of cure to be observed were greater on oxygen permeable windows. This has increased importance for hydrogel resins that require non-contact, optical methods for measuring cure depth, which may be difficult to measure on a printer build plate.[33] These results are important given the prevalence of oxygen permeable materials in 3D printing for reducing adhesive forces to a window or enabling continuous liquid interface printing. The observable depth increase of the oxygen inhibition dead zone with decreasing feature widths could have significant impacts on high resolution 3D printing and warrants further investigation into methods to adapt to this phenomenon. One potential option is to increase the incident light irradiance. However, this may counteract some advantages of oxygen permeable materials, as increasing light irradiance is a common method to mitigate oxygen inhibition in photopolymerization reactions[46] and decreased dead zones with increasing light irradiance has been observed in the literature.[52,54] Here, samples polymerized at 446 mW cm^{-2} on AF 2400 had limited E_c size dependencies, but did not exhibit a measurable dead zone (**Figure S8**).

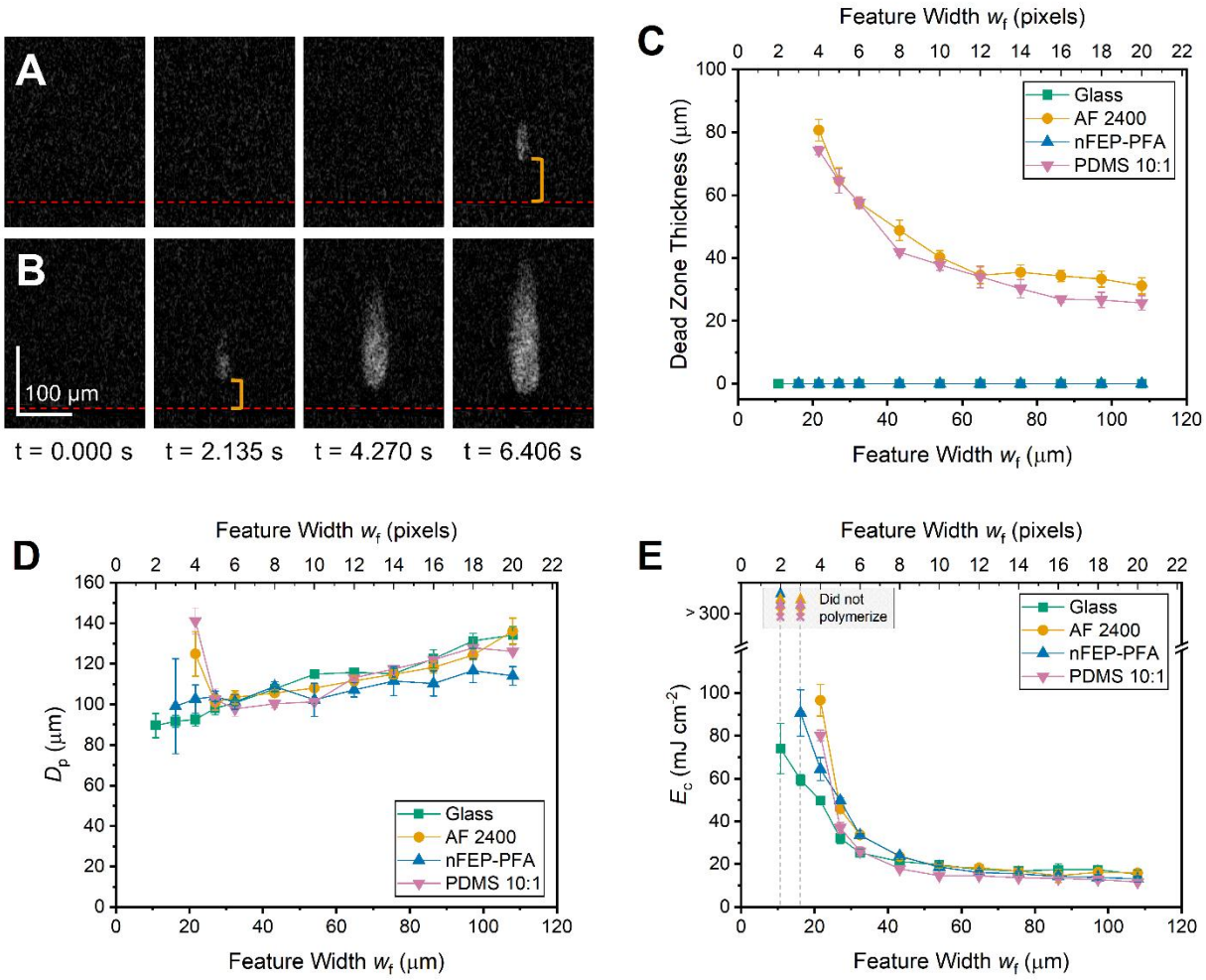

Figure 4. OCT *in situ* imaging enables measurement of photopolymer working curves on various window materials, which exhibit differences from glass slide controls. Representative image sequences of w_f = 27 µm (**A**) and w_f = 54 µm (**B**) features polymerized over AF 2400. Dashed lines indicate the resin-window interface. Scale bars represent 100 µm. **C**) Oxygen dead zone thickness increases as feature width decreases. Comparisons of D_p (**D**) and E_c (**E**) of various feature widths on each material. Arrows represent conditions that did not polymerize during the experimental observation, resulting in E_c greater than 300 mJ cm^{-2}. Data represent mean ± standard deviation of at least four replicates.

Dye Concentration Influences both D_p and E_c

Current approaches to high-resolution printing often make use of low D_p resins. A low D_p resin can be achieved through increased dye/absorber concentrations and results in slower growth of the polymer feature. In other words, small deviations in radiant exposure do not result in large changes to cure depth. However, the addition of dye is not thought to significantly influence the E_c of a resin, as E_c is an extrapolated parameter that describes a property at the substrate-resin interface (i.e., where no light has been absorbed by the resin). Given the relevance of low D_p resins to high-resolution printing, we measured working curves on three different formulations of increasing tartrazine concentrations, a commonly used dye in hydrogel

bioprinting applications due to its water solubility and cytocompatibility.[3,55] Using an incident irradiance of 23 mW cm^{-2}, *in situ* working curves clearly demonstrate the differences in D_p, which are roughly aligned with UV/Vis calculated D_p for each resin (**Figure 5A**, **Table S5**). Notably, E_c was dependent on dye concentration, with increased dye concentration resulting in increased E_c, which is most significant at small w_f (**Figure 5B**, **Table S5**). For example, feature widths below 30 µm were unable to be polymerized during the experimental time for the lowest D_p resin (0.5 % tartrazine by mass). These results are unexpected given the assumption that dyes will only influence a resin's D_p, and are not thought to significantly influence E_c. At the larger feature sizes, one explanation for this observation is that tartrazine can be degraded by radical species[56,57] and as such, could act as a radical scavenger in addition to its role as a light absorber. This could explain the increase in E_c of a similar magnitude to that of window materials PDMS and AF, in which oxygen inhibition of radicals is present. While other dyes used in photopolymer resins may not strongly interact with radicals and thus, be less sensitive to E_c size dependencies, future studies are needed to better understand these systems and describe the underlying mechanisms. The implications of dye concentration on E_c for high resolution printing are perhaps more profound, indicating that while dye loading can improve z-fidelity, it will come at the expense of minimum lateral feature size unless accounted for with larger exposure.

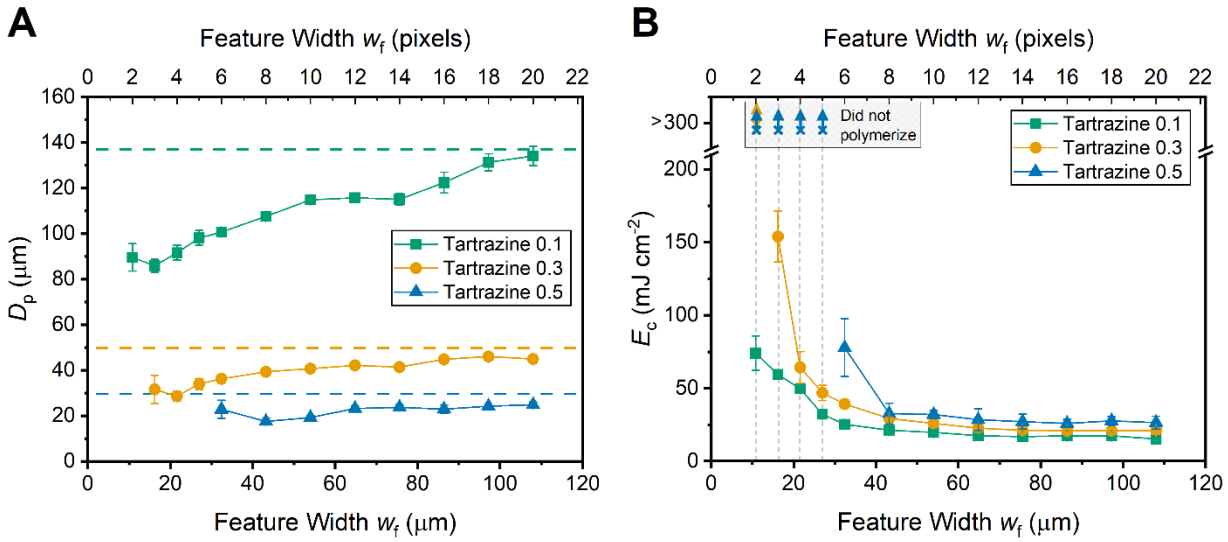

Figure 5. Increasing tartrazine concentration influences both D_p and E_c. **A**) D_p versus Feature Width for hydrogel formulations of increasing tartrazine concentrations. Dashed lines indicate the optical D_p of the resin measured using UV/Vis for each formulation. **B**) E_c versus Feature Width for hydrogel formulations of increasing tartrazine concentrations. Open data points represent conditions that did not polymerize during the experimental observation, resulting in E_c greater than 300 mJ cm^{-2}. Data represent mean ± standard deviation of at least four replicates. Note: Data for tartrazine 0.1 % by mass is same as the Glass control in **Figure 4**.

Print Correction Using Size-Dependent Working Curve Data

Size dependence during photopolymerization presents a challenge to high-resolution 3D printing of hydrogels. However, we can use the developed working curve relationships to begin to correct for these differences. For example, using the extracted D_p and E_c for each feature width and irradiance, an exposure time to reach a specific height can be calculated for a given w_f (**Figure 6A**). The adjusted exposure time can then be programmed with a projected mask pattern, and a corrected print obtained. Here, we demonstrate this correction using two examples. First, we used a bifurcating photomask pattern ranging from $w_f = 108$ μm to $w_f = 10.8$ μm and attempted to polymerize a single-layer to a consistent height of $C_d = 100$ μm using an irradiance of $I_0 = 23$ mW cm^{-2}. Initially, the mask was projected using $E_0 = 138$ mJ cm^{-2} for all feature widths (expected to polymerize the smallest feature to $C_d = 100$ μm). Drastic differences in heights are observed, as the larger w_f feature had significant overcure. Next, the size dependent working curve was used to inform the radiant exposure for different areas of the mask, with larger features having less radiant exposure: $E_0(108\ \mu m) = 29$ mJ cm^{-2}, $E_0(54\ \mu m) = 35$ mJ cm^{-2}, $E_0(27\ \mu m) = 71$ mJ cm^{-2}, $E_0(10.4\ \mu m) = 138$ mJ cm^{-2}. Significantly improved consistency in C_d is observed in the sample using this modified exposure scheme (**Figure 6B**). It should be noted that the projector image stack was binary and was arranged such that all features finished printing at the same time. While the corrected exposure sample was significantly more consistent to the target 100 μm cure depth, some discrepancies were observed. Specifically, at the bifurcation nodes, a larger cure depth was observed, and the smallest features exhibited decaying cure depth as the free end of the feature was approached. These observations are likely due to asymmetry of the lateral boundary (e.g., large-to-small or small-to-no feature transitions) and resulting changes in availability of oxygen for diffusion. Finally, the diagonal line features had a slightly decreased cure depth, although this is likely dominated by the lessened total irradiance of a stair-stepped diagonal versus rectangular region, leading to a square root of two factor reduction in effective width. In the second example, a multi-layer print was designed with the final layer consisting of line patterns ranging from $w_f = 108$ μm down to $w_f = 27$ μm. Layer thicknesses were programmed to 50 μm, and irradiance was set to 20 mW cm^{-2}. Note that the radiant exposures on the printer differ slightly from the projector due to the granularity of control in the printer. There may also be some discrepancy due to the precise illumination pattern of the larger printer pixels (27 μm/pixel) compared to the higher-resolution projector used for *in-situ* OCT (5.4 μm/pixel). Initially, a naïve approach was used to cure all features at $E_0 = 40$ mJ cm^{-2}, sufficient to cure the largest feature in an unbounded experiment to $C_d = 125$ μm deep and easily bridge the 50 μm layer gap. While large features successfully printed and attached to the part, $w_f = 54$ μm features polymerized but exhibited significant delamination, and $w_f = 27$ μm features failed to print at all (**Figure 6C, top)**. The result agreed well with the working curves wherein $w_f = 108$ μm and $w_f = 81$ μm features are predicted to bridge the 50 μm layer, $w_f = 54$ μm features should minimally bridge the layer, and $w_f = 27$ μm were predicted to fail to bridge the layer (i.e. print failure). The informed print utilized corrected exposures to bridge the layer gap. Based on the size dependent working curve, $E_0(108\ \mu m) = 40$ mJ cm^{-2}, $E_0(81\ \mu m) = 40$ mJ cm^{-2}, $E_0(54\ \mu m) = 60$ mJ cm^{-2}, $E_0(27\ \mu m) = 80$ mJ cm^{-2} were used. Here, all features successfully printed and attached to the part (**Figure 6C, bottom)**. Although OCT artifacts have not been ruled out, a notable observation is that the features appear to detectably penetrate the previous layer(s) of the part. The ability to detect cure-through non-destructively could further inform future

optimization studies, particularly if coupled with evidence of delamination such as was observed for the naïve $w_f = 54$ µm features.

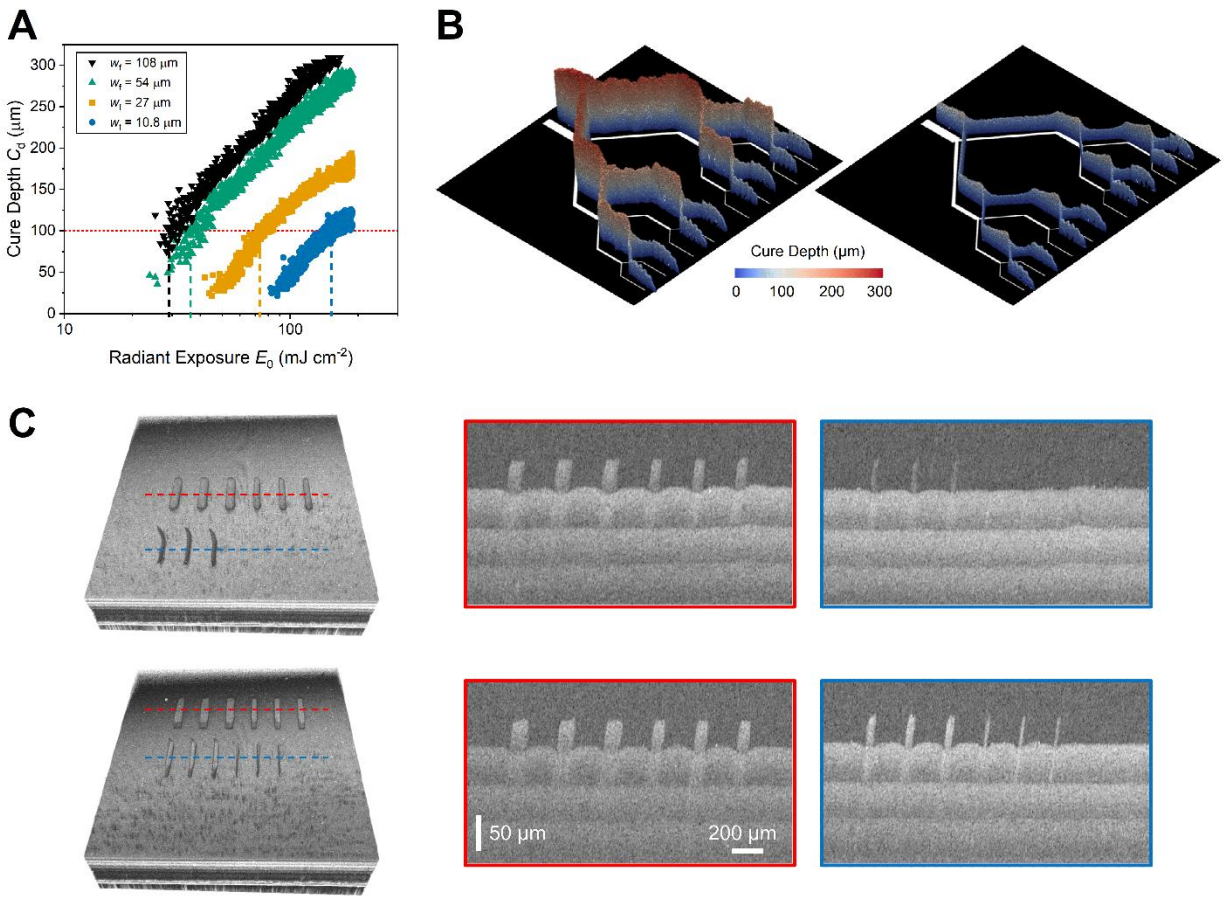

Figure 6. Quantification of hydrogel size dependent working curve enables correction of cure depth based on feature width. (**A**) Representative working curves of $w_f = 108$ µm, $w_f = 54$ µm, $w_f = 27$ µm, and $w_f = 10.4$ µm features demonstrate the different radiant exposures needed to reach a cure depth of 100 µm (dashed red line). (**B**) Naïve (left) and corrected (right) single-layer bifurcating structure demonstrating height differences based on feature widths. Naïve structure had a constant radiant exposure of $E_0 = 138$ mJ cm^{-2}. The corrected structure had exposures calculated from the working curve of each feature width: E_0(108 µm) = 29 mJ cm^{-2}, E_0(54 µm) = 35 mJ cm^{-2}, E_0(27 µm) = 71 mJ cm^{-2}, E_0(10.4 µm) = 138 mJ cm^{-2}. (**C**) 3D renderings and cross-sectional images of naïve (top) and corrected (bottom) multi-layer 3D printed structures with features of widths 4 pixels ($w_f = 108$ µm), 3 pixels ($w_f = 81$ µm), 2 pixels ($w_f = 54$ µm), and 1 pixel ($w_f = 27$ µm). Naïve print had a constant exposure of $E_0 = 40$ mJ cm^{-2} while the corrected structure had irradiances based on the working curve of each feature width: E_0 (108 µm) = 40 mJ cm^{-2}, E_0(81 µm) = 40 mJ cm^{-2}, E_0(54 µm) = 60 mJ cm^{-2}, E_0(27 µm) = 80 mJ cm^{-2}.

Implications of size dependence in hydrogel printing

Given the complex architecture of native tissues, and the inherent connection between form and function, ensuring design fidelity in high-resolution hydrogel printing is vital to advance biomedical research. While this study focused on one polymer class (PEGDA), the results are expected to be generalized to many hydrogel compositions, given that diffusional properties of the resin are likely dominated by their high-water content. As vat polymerization seeks to produce increasingly smaller features into increasingly larger parts, a fundamental understanding of size dependence of voxel formation will gain more importance. The fact that E_c values can increase an order of magnitude or more in small features compared to large features poses opportunities for both materials and process researchers. A critical challenge is that faithful production of visibly resolved features does not ensure comparable fidelity of smaller or closer spaced features. While the implications of size dependence on voxel scale geometric precision are clear, the impacts on properties could also be important. For example, exposures that inadvertently overcure large features could result in higher modulus and reduced species diffusion. Likewise, undercured features could be undesirably weak in green strength, resulting in failed prints. Precisely forming each voxel with a specified exposure to achieve a desired cure depth will lead to higher performing, more reliable structures and devices. The fact that size dependence can be mitigated at high irradiances should motivate efforts towards higher powered light engines; however, tradeoffs such as the reduction in dead zone thickness and corresponding increase in adhesive Stefan force must be carefully balanced.

The above discussion of size dependence suggests a broader investigation into more complex lateral boundary conditions. For example, the digital projector enables a range of planar geometries such as annuli, curves, and other arbitrary shapes to be explored. Furthermore, the depth imaging capabilities of the OCT apparatus naturally lend themselves to studies of vertical boundary conditions (e.g. printing into void space) which are more representative of multilayer 3D printing. Finally, the 3D imaging modality of the OCT as demonstrated in Figure 6 can also be time-resolved to inform 3D multiphysics models of the printing process. It should be noted that the method presented is reliant on inks that exhibit a large contrast change during gelation. Here, that is achieved with the addition of alginate, which phase separates from the PEGDA upon gelation. Because not all inks will deliver sufficient contrast for highspeed imaging, the limits of both material and instrument optimization for maximum signal should be explored.

3. Conclusion

The curing kinetics of hydrogel bioinks, as revealed by *in situ* working curve measurements, exhibited extreme dependence on exposure, formulation, and window conditions. Unlike traditional working curves that are measured *ex situ* on millimeter-scale features, our measurements employed optical coherence tomography to observe voxel formation and the working curve in real time on features down to only 10.8 μm in width. At low irradiances typical of LCD and DLP printers, E_c values increase an order of magnitude or more when feature width is reduced from 108 μm to 10.8 μm. Higher irradiances up to nearly 500 mW cm^{-2} greatly

reduced this size sensitivity, but proved to be less photon-efficient, driving up the E_c values for larger features. The novel use of *in situ* OCT imaging enabled the observation of polymerization, size dependence, and dead zone thickness when printing with oxygen permeable windows. The size dependent working curves can be used as a model to ensure print fidelity regardless of feature size, as demonstrated on both single- and multi-layer prints. Overall, size dependence must be a consideration for future progress in high-resolution vat photopolymerization of hydrogels.

4. Materials and Methods

Certain commercial equipment, instruments, or materials are identified in this paper to specify the experimental procedure adequately. Such identification is not intended to imply recommendation or endorsement by NIST.

4.1 Materials

Polyethylene glycol diacrylate (PEGDA, M_w = 700 Da), sodium alginate, and tartrazine were purchased from Sigma Aldrich (St. Louis, MO, USA). The photoinitiator lithium phenyl-2,4,6-trimethylbenzoylphosphinate (LAP) was purchased from AmBeed, Inc. (Arlington Heights, IL, USA). All chemicals were used as received.

4.2 Hydrogel Formulations

Water-based hydrogel formulations were used for all experimentation. The primary formulation consisted of 10 % by mass PEGDA 700 in deionized water with 0.5 % by mass sodium alginate. Alginate was added to the formulation to increase the phase separation (imaging contrast) of polymerized structures and is necessary for fast, real-time imaging. Without alginate, the sampling rate and averaging required to obtain resolved images of the hydrogel structures are on the order of 1 Hz to 5 Hz rather than roughly 100 Hz in these experiments. Additionally, alginate was chosen as it is a commonly used hydrogel material across a variety of biomedical applications, often added to reach desired mechanical or biological properties.[58,59] The hydrogel formulation contained photoinitiator LAP at 0.5 % by mass and photoabsorber tartrazine at 0.1 % by mass. For some experiments, the concentration of tartrazine was increased to 0.3 % by mass or 0.5 % by mass. Formulations were stored protected from light prior to use.

4.3 In situ OCT instrument

4.3.1 Light Engine

To photopolymerize the hydrogel samples, a Luxbeam Rapid System projector (Visitech) was situated under a movable stage and the OCT head (**Figure 8A**). The projector had a 1920 x 1080-

pixel resolution using a nominal 385 nm light output and a 0.5x lens, which resulted in pixel ratio of 5.4 μm. The projector was connected to the OCT computer via an analog input to ensure accurate timing of light exposure was recorded. The projector photospectrum was characterized using a spectrometer (Avantes, AvaSpec-ULS4096CL-EVO) showing a maximum emission at 384 nm with a full width half max of roughly 9 nm (**Figure 8B**). The irradiance of the projector at each power level tested was calibrated using an integrating sphere photodiode power meter (S142C, Thorlabs) and ranged from roughly 5 mW cm^{-2} to 450 mW cm^{-2} (**Figure 8C**).

Photomasks were generated as 1920 x 1080 bitmap images with a variety of feature patterns. All *in situ* experiments were composed of 5 features with specified feature width w_f and feature spacing s_f (**Figure 1A**). For varying w_f experiments, features of (2, 3, 4, 5, 6, 8, 10, 12, 14, 16, 18, and 20) pixels wide (a range of 10.8 μm to 108 μm) were spaced 100 pixels (s_f = 540 μm) apart to minimize the influence of feature-to-feature interactions. For feature spacing s_f experiments, features 2 pixels and 20 pixels wide were spaced (1, 2, 3, 4, 5, 10, 15, 20, 30, and 50) pixels apart (a range of 5.4 μm to 270 μm). Using the same spacing pattern, masks were also made with alternating 2 pixel and 20 pixel wide features. The bifurcating sample mask consisted of four feature width levels of (2, 5, 10, and 20) pixels.

4.3.2 Optical Coherence Tomography (OCT) Apparatus

OCT is a non-invasive imaging technique which uses near-infrared light to detect contrast from differences in light scattering throughout a sample. Here, an OCT (Thorlabs Ganymede, 880 nm, GAN632C1) system was used to obtain images of hydrogel samples during exposure to light. OCT images were collected at 200 kHz without A-scan or B-scan averages to maximize temporal resolution across the experimental field of view. The x-resolution of the scale was set to 1.5 μm per pixel. The z-scale of OCT images is dependent on the refractive index of the sample. As such, the refractive index of the hydrogel resin and polymerized sample were calculated using a reference height imaged through air (refractive index of 1.00) and water (refractive index of 1.33).[33] The refractive index both the hydrogel resin and polymerized sample was determined to be 1.35, giving a z-scale of 1.19 μm per pixel. It should be noted that OCT is accurate and comparable to other methods of measuring sample heights or thicknesses.[60] In this study, the accuracy of OCT was confirmed using an *ex situ* approach. Samples were polymerized with three different exposure durations (S1, S2 and S3) on a glass slide and the cure depth measured using only the resulting OCT contrast of the hydrogel. Tungsten beads (nominal diameter of 12 μm, Sigma Aldrich) were then added on top of the same samples to create a higher contrast outline (**Figure 8D-E**). The cure depth measured using just the sample contrast had no significant differences from the cure depth measured using tungsten beads as contrast agents, indicating the *in situ* measurements of cure depth are accurate and that sample contrast is indicative of gelation (**Figure 8F**).

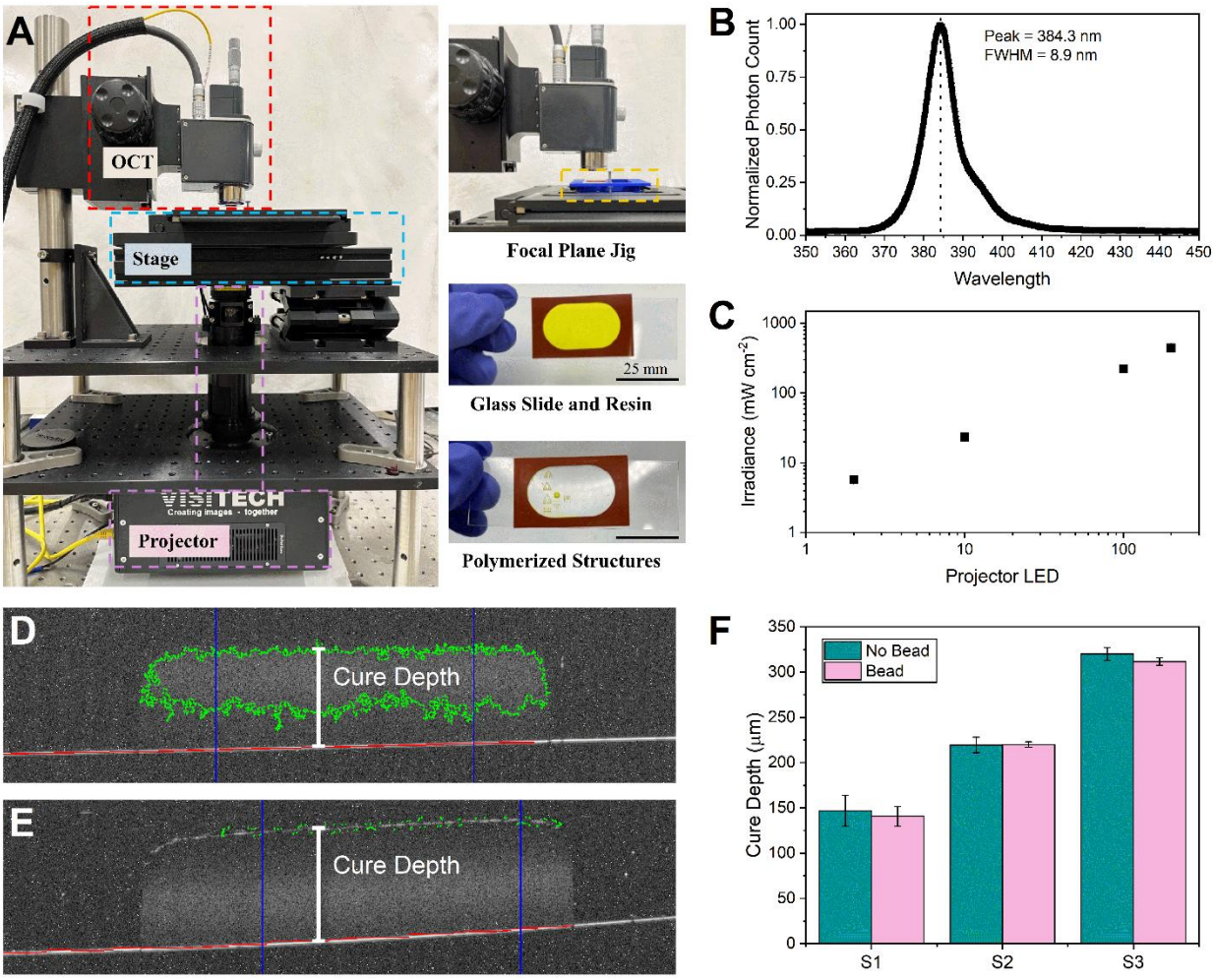

Figure 8. Characterization of experimental setup. **A**) Image depicting the alignment of the OCT and projector including the focal plane jig, as well as the glass slide and silicone isolator to contain the resin volume. **B**) Projector light spectrum centered around 384 nm. **C**) Calibration of arbitrary projector LED power levels. **D**) Representative OCT image of measuring the cure depth of a sample using only sample contrast. Green trace represents the automated detection of the sample, with the cure depth measured as the average distance from the glass slide interface (red line) to the top of the sample. **E**) Representative image of measuring the cure depth of a sample using tungsten beads as a contrast enhancing outline. Green trace represents the tungsten beads. **F**) No significant difference is observed between the cure depth measured using sample contrast versus tungsten beads for 3 different cure depths (S1, S2 and S3).

4.3.3 Experimental Setup and Workflow

To measure real time photopolymerization of the hydrogel samples, the OCT was placed over the projector (**Figure 1A**). Hydrogel resins were polymerized onto glass slides functionalized with 3-(trimethoxysilyl) propyl methacrylate (Automate Scientific; Berkeley, CA, USA). Resin was contained using 400 µm thick silicone isolators (Grace Biolabs; Bend, OR) and a coverslip. Alternatively, some experiments were conducted on oxygen permeable materials; here the glass slide was replaced either with 10:1 base-to-curing agent ratio of PDMS (Sylgard 184), Teflon

amorphous fluoropolymer (AF 2400; Kodak, Rochester. NY), or perfluoroalkoxy film (nFEP-PFA; Phrozen, Hsinchu City, Taiwan). Prior to imaging, the focal plane of the projector and OCT were aligned to the printing interface. To do this, a custom jig was fabricated to tilt the glass slide relative to the projector and OCT focal plane (**Figure 8A**). This enabled a larger range of stage heights to be tested in a single exposure, reducing the time required to step through single focal plane trials. Line patterns were then displayed on the projector, and the focal plane adjusted until the sharpest feature was polymerized, roughly corresponding to the pixel scaling of the projector (e.g., a 5-pixel wide mask should polymerize a feature with a width of 27 μm). Once the optimal focal plane was determined, the slide was moved to a level, horizontal orientation, and the projector displayed line patterns of various widths and spacings while OCT images were collected over the exposure. To ensure accurate timing data, "3D mode" was used to collect OCT images, with the zero-size y-direction set to collect images over time.

OCT data was then analyzed using IMPPY3D software in Python[61] to determine cure depth for different radiant exposure and construct working curves for the various pattern conditions. Briefly, the last image in the OCT sequence was used to identify a bounding box around the polymerized features. Image denoising, filtering, normalizing, and background subtraction (background calculated from frames prior to light exposure) was then performed on the image sequence. To determine the cure depths of the polymerized features, the average and standard deviation of the baseline pixel value for each bounding box was determined (defined as frames prior to light exposure). The baseline threshold was set to the average pixel value plus three times the standard deviation. Next, the average pixel value of each row in the feature bounding box was calculated. The last row of the bounding box that had an average pixel value greater than baseline threshold for a given frame was set to be the height of the feature (**Figure 1B**). Performing this calculation across the image sequence (rescaling the row numbers by the OCT z-scale and frame numbers by the OCT timing and projector irradiance) gives a working curve relationship of cure depth C_d versus radiant exposure E_0. Given possible noise in the OCT imaging, a random sample consensus (RANSAC) regression[62] was performed to exclude outliers and fit the Jacobs model to the working curve data (**Figure 1C**).

4.4 Digital Light Processing 3D Printing

A DLP printer (ASIGA MAX X) with 385 nm nominal wavelength and 27 μm pixel resolution was used to fabricate hydrogel structures. Bitmap photomask images for each 50 μm layer were generated for sequential exposure using an irradiance of 20 mW cm^{-2}. The first three (burn in) layers had a radiant exposure E_0 = 160 mJ cm^{-2} while sequential part layers were polymerized with E_0 = 80 mJ cm^{-2}. For the last layer with various feature sizes (w_f = 108 μm to w_f = 27 μm) the naïve print had a constant E_0 = 40 mJ cm^{-2} while the size dependent corrected print had variable radiant exposures: E_0(108 μm) = 40 mJ cm^{-2}, E_0(81 μm) = 40 mJ cm^{-2}, E_0(54 μm) = 60 mJ cm^{-2}, E_0(27 μm) = 80 mJ cm^{-2}. Note that these radiant exposures are not explicitly equivalent to the OCT working curves, based on the granularity of the settings for printer exposures.

Data Availability:

Analysis code and example OCT data are available at https://doi.org/10.18434/mds2-4006. Due to file sizes, further data are available upon request.

CRediT Authorship Contribution Statement:

RJW: Conceptualization, Data curation, Formal analysis, Investigation, Methodology, Software, Validation, Visualization, Writing – Original Draft, Writing – Review and Editing.

OLK: Conceptualization, Data Curation, Investigation, Methodology, Software, Writing – Review and Editing.

TJK: Investigation, Methodology, Writing – Review and Editing.

CIH: Resources, Writing – Review and Editing.

GD: Resources, Methodology.

NC: Methodology, Resources.

RLS: Conceptualization, Methodology, Validation.

KV: Validation, Methodology, Resources.

DB: Conceptualization, Methodology, Resources, Project administration, Funding acquisition.

AK: Methodology, Resources.

MG: Conceptualization, Investigation, Methodology, Resources.

MB: Methodology, Resources.

ST: Conceptualization, Methodology, Resources, Project administration, Funding acquisition.

JPK: Conceptualization, Funding acquisition, Investigation, Methodology, Project administration, Resources, Supervision, Visualization, Writing – Review and Editing.

Acknowledgements:

This work was performed while Rion Wendland held a National Research Council Associateship Award at the National Institute of Standards and Technology.

References

(1) Tabatabaei Rezaei, N.; Kumar, H.; Liu, H.; Lee, S. S.; Park, S. S.; Kim, K. Recent Advances in Organ-on-Chips Integrated with Bioprinting Technologies for Drug Screening. *Advanced Healthcare Materials* **2023**, *12* (20), 2203172. https://doi.org/10.1002/adhm.202203172.

(2) Jiang, Z.; Jin, B.; Liang, Z.; Wang, Y.; Ren, S.; Huang, Y.; Li, C.; Sun, H.; Li, Y.; Liu, L.; Li, N.; Wang, J.; Cui, Z.; Huang, P.; Yang, H.; Mao, Y.; Ye, H. Liver Bioprinting within a Novel Support Medium with Functionalized Spheroids, Hepatic Vein Structures, and Enhanced Post-Transplantation Vascularization. *Biomaterials* **2024**, *311*, 122681. https://doi.org/10.1016/j.biomaterials.2024.122681.

(3) Grigoryan, B.; Paulsen, S. J.; Corbett, D. C.; Sazer, D. W.; Fortin, C. L.; Zaita, A. J.; Greenfield, P. T.; Calafat, N. J.; Gounley, J. P.; Ta, A. H.; Johansson, F.; Randles, A.; Rosenkrantz, J. E.; Louis-Rosenberg, J. D.; Galie, P. A.; Stevens, K. R.; Miller, J. S. Multivascular Networks and Functional Intravascular Topologies within Biocompatible Hydrogels. *Science* **2019**, *364* (6439), 458–464. https://doi.org/10.1126/science.aav9750.

(4) Saraswathibhatla, A.; Indana, D.; Chaudhuri, O. Cell-Extracellular Matrix Mechanotransduction in 3D. *NATURE REVIEWS MOLECULAR CELL BIOLOGY* **2023**, *24* (7), 495–516. https://doi.org/10.1038/s41580-023-00583-1.

(5) Dienemann, S.; Schmidt, V.; Fleischhammer, T.; Mueller, J. H.; Lavrentieva, A. Comparative Analysis of Hypoxic Response of Human Microvascular and Umbilical Vein Endothelial Cells in 2D and 3D Cell Culture Systems. *Journal of Cellular Physiology* **2023**, *238* (5), 1111–1120. https://doi.org/10.1002/jcp.31002.

(6) Biju, T. S.; Priya, V. V.; Francis, A. P. Role of Three-Dimensional Cell Culture in Therapeutics and Diagnostics: An Updated Review. *Drug Deliv. and Transl. Res.* **2023**, *13* (9), 2239–2253. https://doi.org/10.1007/s13346-023-01327-6.

(7) Fleischer, S.; Tavakol, D. N.; Vunjak-Novakovic, G. From Arteries to Capillaries: Approaches to Engineering Human Vasculature. *Advanced Functional Materials* **2020**, *30* (37), 1910811. https://doi.org/10.1002/adfm.201910811.

(8) Neelakantan, S.; Xin, Y.; Gaver, D. P.; Cereda, M.; Rizi, R.; Smith, B. J.; Avazmohammadi, R. Computational Lung Modelling in Respiratory Medicine. *Journal of The Royal Society Interface* **2022**, *19* (191), 20220062. https://doi.org/10.1098/rsif.2022.0062.

(9) Killgore, J. P.; Kolibaba, T. J.; Caplins, B. W.; Higgins, C. I.; Rezac, J. D. A Data-Driven Approach to Complex Voxel Predictions in Grayscale Digital Light Processing Additive Manufacturing Using U-Nets and Generative Adversarial Networks. *Small* **2023**, *19* (50), 2301987. https://doi.org/10.1002/smll.202301987.

(10) Sun, C.; Fang, N.; Wu, D. M.; Zhang, X. Projection Micro-Stereolithography Using Digital Micro-Mirror Dynamic Mask. *Sensors and Actuators A: Physical* **2005**, *121* (1), 113–120. https://doi.org/10.1016/j.sna.2004.12.011.

(11) Chandler, C.; Porcincula, D. H.; Ford, M. J.; Kolibaba, T. J.; Fein-Ashley, B.; Brodsky, J.; Killgore, J. P.; Sellinger, A. Influence of Fluorescent Dopants on the Vat Photopolymerization of Acrylate-Based Plastic Scintillators for Application in Neutron/Gamma Pulse Shape Discrimination. *Additive Manufacturing* **2023**, *73*, 103688. https://doi.org/10.1016/j.addma.2023.103688.

(12) Camposeo, A.; Arkadii, A.; Romano, L.; D'Elia, F.; Fabbri, F.; Zussman, E.; Pisignano, D. Impact of Size Effects on Photopolymerization and Its Optical Monitoring *in-Situ*. *Additive Manufacturing* **2022**, *58*, 103020. https://doi.org/10.1016/j.addma.2022.103020.

(13) Orth, A.; Webber, D.; Zhang, Y.; Sampson, K. L.; de Haan, H. W.; Lacelle, T.; Lam, R.; Solis, D.; Dayanandan, S.; Waddell, T.; Lewis, T.; Taylor, H. K.; Boisvert, J.; Paquet, C. Deconvolution

Volumetric Additive Manufacturing. *Nat Commun* **2023**, *14* (1), 4412. https://doi.org/10.1038/s41467-023-39886-4.
(14) Brown, T. E.; Malavé, V.; Higgins, C. I.; Kotula, A. P.; Caplins, B. W.; Garboczi, E. J.; Killgore, J. P. Voxel-Scale Conversion Mapping Informs Intrinsic Resolution in Stereolithographic Additive Manufacturing. *ACS Appl. Polym. Mater.* **2021**, *3* (1), 290–298. https://doi.org/10.1021/acsapm.0c01090.
(15) Torres-Alvarez, D.; Celis-Guzman, A.; Aguirre-Soto, A. Resin-Dependent Mechanical Anisotropy in Laser Vat Photopolymerization Correlates to the Initial Rate of Polymerization and Critical Energy. *Additive Manufacturing Letters* **2025**, *12*, 100264. https://doi.org/10.1016/j.addlet.2024.100264.
(16) Rudenko, Yu.; Lozovaya, A.; Asanova, L.; Fedyakova, N.; Chapala, P. Light Intensity Influence on Critical Energy and Penetration Depth for Vat Photopolymerization Technology. *Prog Addit Manuf* **2024**, *9* (2), 553–561. https://doi.org/10.1007/s40964-023-00474-z.
(17) Rudenko, Y.; Prosyankin, E.; Mustafina, A.; Fuki, M.; Borisov, R.; Fedyakova, N.; Bermeshev, M.; Chapala, P. Investigation of the Light Intensity and Temperature Influences on Double Bond Conversion in Resins for Vat Photopolymerization via Fourier Transform Infrared Spectroscopy. *MACROMOLECULAR CHEMISTRY AND PHYSICS* **2025**, *226* (9). https://doi.org/10.1002/macp.202400398.
(18) Uzcategui, A. C.; Higgins, C. I.; Hergert, J. E.; Tomaschke, A. E.; Crespo-Cuevas, V.; Ferguson, V. L.; Bryant, S. J.; McLeod, R. R.; Killgore, J. P. Microscale Photopatterning of Through-Thickness Modulus in a Monolithic and Functionally Graded 3D-Printed Part. *Small Sci* **2021**, *1* (3), 2000017. https://doi.org/10.1002/smsc.202000017.
(19) Billerbeck, K.; Hägele, C.; Träger, J. Relation of the Working Curve and Exposure Intensity in VPP 3D-Printing. *Prog Addit Manuf* **2024**, *9* (4), 1015–1023. https://doi.org/10.1007/s40964-023-00498-5.
(20) Bennett, J. Measuring UV Curing Parameters of Commercial Photopolymers Used in Additive Manufacturing. *Additive Manufacturing* **2017**, *18*, 203–212. https://doi.org/10.1016/j.addma.2017.10.009.
(21) Kardar, P.; Ebrahimi, M.; Bastani, S. Influence of Temperature and Light Intensity on the Photocuring Process and Kinetics Parameters of a Pigmented UV Curable System. *J Therm Anal Calorim* **2014**, *118* (1), 541–549. https://doi.org/10.1007/s10973-014-3984-z.
(22) Luu, T. T. H.; Jia, Z.; Kanaev, A.; Museur, L. Effect of Light Intensity on the Free-Radical Photopolymerization Kinetics of 2-Hydroxyethyl Methacrylate: Experiments and Simulations. *J. Phys. Chem. B* **2020**, *124* (31), 6857–6866. https://doi.org/10.1021/acs.jpcb.0c03140.
(23) Madrid-Wolff, J.; Boniface, A.; Loterie, D.; Delrot, P.; Moser, C. Controlling Light in Scattering Materials for Volumetric Additive Manufacturing. *ADVANCED SCIENCE* **2022**, *9* (22). https://doi.org/10.1002/advs.202105144.
(24) Guan, J.; You, S.; Xiang, Y.; Schimelman, J.; Alido, J.; Ma, X.; Tang, M.; Chen, S. Compensating the Cell-Induced Light Scattering Effect in Light-Based Bioprinting Using Deep Learning. *BIOFABRICATION* **2022**, *14* (1). https://doi.org/10.1088/1758-5090/ac3b92.
(25) Montgomery, S. M.; Hamel, C. M.; Skovran, J.; Qi, H. J. A Reaction–Diffusion Model for Grayscale Digital Light Processing 3D Printing. *Extreme Mechanics Letters* **2022**, *53*, 101714. https://doi.org/10.1016/j.eml.2022.101714.
(26) Ma, Y.; Tian, Z.; Wang, B.; Zhao, Y.; Nie, Y.; Wildman, R. D.; Li, H.; He, Y. Enhancing the 3D Printing Fidelity of Vat Photopolymerization with Machine Learning-Driven Boundary Prediction. *Materials & Design* **2024**, *241*, 112978. https://doi.org/10.1016/j.matdes.2024.112978.

(27) Berry, B. C.; Stafford, C. M.; Pandya, M.; Lucas, L. A.; Karim, A.; Fasolka, M. J. Versatile Platform for Creating Gradient Combinatorial Libraries via Modulated Light Exposure. *Rev Sci Instrum* **2007**, *78* (7), 072202. https://doi.org/10.1063/1.2755729.
(28) Jacobs, P. F. *Fundamentals of Stereolithography*; 1992.
(29) Chivate, A.; Zhou, C. Enhanced Schlieren System for In Situ Observation of Dynamic Light–Resin Interactions in Projection-Based Stereolithography Process. *J. Manuf. Sci. Eng* **2023**, *145* (081005). https://doi.org/10.1115/1.4062218.
(30) Khitous, A.; Lartigue, L.; Moreau, J.; Soppera, O. Insights into Photopolymerization at the Nanoscale Using Surface Plasmon Resonance Imaging. *Small* **2024**, *20* (40), 2401885. https://doi.org/10.1002/smll.202401885.
(31) Orth, A.; Sampson, K. L.; Zhang, Y.; Ting, K.; van Egmond, D. A.; Laqua, K.; Lacelle, T.; Webber, D.; Fatehi, D.; Boisvert, J.; Paquet, C. On-the-Fly 3D Metrology of Volumetric Additive Manufacturing. *Additive Manufacturing* **2022**, *56*, 102869. https://doi.org/10.1016/j.addma.2022.102869.
(32) Fiedler-Higgins, C. I.; Cox, L. M.; DelRio, F. W.; Killgore, J. P. Monitoring Fast, Voxel-Scale Cure Kinetics via Sample-Coupled-Resonance Photorheology. *Small Methods* **2019**, *3* (2), 1800275. https://doi.org/10.1002/smtd.201800275.
(33) Wendland, R. J.; Kolibaba, T. J.; Worthington, K. S.; Killgore, J. P. A Practical Guide to Hydrogel Working Curves for Bioprinting. *Additive Manufacturing Letters* **2025**, *14*, 100293. https://doi.org/10.1016/j.addlet.2025.100293.
(34) Sekmen, K.; Rehbein, T.; Johlitz, M.; Lion, A.; Constantinescu, A. Thermal Analysis and Shrinkage Characterization of the Photopolymers for DLP Additive Manufacturing Processes. *Continuum Mech. Thermodyn.* **2024**, *36* (2), 351–368. https://doi.org/10.1007/s00161-022-01137-0.
(35) Amrin Luna, J.; Cho, H.; Son, K.; Lee, J.-M.; Abu Saleah, S.; Seong, D.; Han, S.; Lee, K.-B.; Jeon, M.; Kim, J. Assessment of Temperature Effects on Photopolymer Resin Dental Prosthetics Fabricated by Stereolithography Using Optical Coherence Tomography. *Optics & Laser Technology* **2024**, *179*, 111248. https://doi.org/10.1016/j.optlastec.2024.111248.
(36) Tashman, J. W.; Shiwarski, D. J.; Coffin, B.; Ruesch, A.; Lanni, F.; Kainerstorfer, J. M.; Feinberg, A. W. In Situ Volumetric Imaging and Analysis of FRESH 3D Bioprinted Constructs Using Optical Coherence Tomography. *Biofabrication* **2022**, *15* (1), 014102. https://doi.org/10.1088/1758-5090/ac975e.
(37) Wang, L.; Xu, M.; Zhang, L.; Zhou, Q.; Luo, L. Automated Quantitative Assessment of Three-Dimensional Bioprinted Hydrogel Scaffolds Using Optical Coherence Tomography. *Biomed Opt Express* **2016**, *7* (3), 894–910. https://doi.org/10.1364/BOE.7.000894.
(38) Lipkowitz, G.; Samuelsen, T.; Hsiao, K.; Lee, B.; Dulay, M.; Coates, I.; Lin, H.; Pan, W.; Toth, G.; Tate, L.; Shaqfeh, E.; DeSimone, J. Injection Continuous Liquid Interface Production of 3D Objects. *SCIENCE ADVANCES* **2022**, *8* (39). https://doi.org/10.1126/sciadv.abq3917.
(39) Lipkowitz, G.; Coates, I.; Krishna, N.; Shaqfeh, E. S. G.; DeSimone, J. M. Methods for Modeling and Real-Time Visualization of CLIP and iCLIP-Based 3D Printing. *Giant* **2024**, *17*, 100239. https://doi.org/10.1016/j.giant.2024.100239.
(40) Xing, W.; Yin, M.; Lv, Q.; Hu, Y.; Liu, C.; Zhang, J. 1 - Oxygen Solubility, Diffusion Coefficient, and Solution Viscosity. In *Rotating Electrode Methods and Oxygen Reduction Electrocatalysts*; Xing, W., Yin, G., Zhang, J., Eds.; Elsevier: Amsterdam, 2014; pp 1–31. https://doi.org/10.1016/B978-0-444-63278-4.00001-X.
(41) Shimada, K.; Kato, H.; Saito, T.; Matsuyama, S.; Kinugasa, S. Precise Measurement of the Self-Diffusion Coefficient for Poly(Ethylene Glycol) in Aqueous Solution Using Uniform Oligomers. *J Chem Phys* **2005**, *122* (24), 244914. https://doi.org/10.1063/1.1948378.

(42) Waggoner, R. A.; Blum, F. D.; Lang, J. C. Diffusion in Aqueous Solutions of Poly(Ethylene Glycol) at Low Concentrations. *Macromolecules* **1995**, *28* (8), 2658–2664. https://doi.org/10.1021/ma00112a010.
(43) Favre, E.; Leonard, M.; Laurent, A.; Dellacherie, E. Diffusion of Polyethyleneglycols in Calcium Alginate Hydrogels. *Colloids and Surfaces A: Physicochemical and Engineering Aspects* **2001**, *194* (1), 197–206. https://doi.org/10.1016/S0927-7757(01)00789-0.
(44) Wight, F. R. Oxygen Inhibition of Acrylic Photopolymerization. *Journal of Polymer Science: Polymer Letters Edition* **1978**, *16* (3), 121–127. https://doi.org/10.1002/pol.1978.130160304.
(45) Dobson, A. L.; Bowman, C. N. A Comprehensive, Multidimensional First-Principles Model for Free-Radical Photopolymerizations in Bulk and Thin Films. *Advanced Functional Materials* **2024**, *34* (22), 2312607. https://doi.org/10.1002/adfm.202312607.
(46) Ligon, S. C.; Husár, B.; Wutzel, H.; Holman, R.; Liska, R. Strategies to Reduce Oxygen Inhibition in Photoinduced Polymerization. *Chem. Rev.* **2014**, *114* (1), 557–589. https://doi.org/10.1021/cr3005197.
(47) Chivate, A.; Guo, Z.; Zhou, C. Study of Proximity Effect in Projection Based Micro Vat Photopolymerization Process. *Additive Manufacturing* **2024**, *79*, 103926. https://doi.org/10.1016/j.addma.2023.103926.
(48) Drobecq, I.; Bigot, C.; Soppera, O.; Malaquin, L.; Venzac, B. Optimizing Dimensional Accuracy in Two-Photon Polymerization: Influence of Energy Dose and Proximity Effects on Sub-Micrometric Fiber Structures. *Additive Manufacturing* **2025**, *103*, 104735. https://doi.org/10.1016/j.addma.2025.104735.
(49) Kim, H.; Pingali, R.; Saha, S. K. Rapid Printing of Nanoporous 3D Structures by Overcoming the Proximity Effects in Projection Two-Photon Lithography. *Virtual and Physical Prototyping* **2023**, *18* (1), e2230979. https://doi.org/10.1080/17452759.2023.2230979.
(50) Xue, D.; Wang, Y.; Mei, D. Multi-Step Exposure Method for Improving Structure Flatness in Digital Light Processing-Based Printing. *Journal of Manufacturing Processes* **2019**, *39*, 106–113. https://doi.org/10.1016/j.jmapro.2019.02.013.
(51) Anand, G. A. E.; Dam-Hansen, C.; Jensen, O. B.; Pedersen, H. C.; Chang, B.; Liu, X.; Han, A.; Spangenberg, J.; Pedersen, D. B. Vat Photopolymerization Using Pulsed Exposure. *Micro and Nano Engineering* **2025**, *28*, 100311. https://doi.org/10.1016/j.mne.2025.100311.
(52) Tumbleston, J.; Shirvanyants, D.; Ermoshkin, N.; Janusziewicz, R.; Johnson, A.; Kelly, D.; Chen, K.; Pinschmidt, R.; Rolland, J.; Ermoshkin, A.; Samulski, E.; DeSimone, J. Continuous Liquid Interface Production of 3D Objects. *SCIENCE* **2015**, *347* (6228), 1349–1352. https://doi.org/10.1126/science.aaa2397.
(53) Pan, Y.; He, H.; Xu, J.; Feinerman, A. Study of Separation Force in Constrained Surface Projection Stereolithography. *Rapid Prototyping Journal* **2017**, *23* (2), 353–361. https://doi.org/10.1108/RPJ-12-2015-0188.
(54) Kunwar, P.; Xiong, Z.; Mcloughlin, S. T.; Soman, P. Oxygen-Permeable Films for Continuous Additive, Subtractive, and Hybrid Additive/Subtractive Manufacturing. *3D Printing and Additive Manufacturing* **2020**, *7* (5), 216–221. https://doi.org/10.1089/3dp.2019.0166.
(55) Pariskar, A.; Sharma, P. K.; Murty, U. S.; Banerjee, S. Effect of Tartrazine as Photoabsorber for Improved Printing Resolution of 3D Printed "Ghost Tablets": Non-Erodible Inert Matrices. *Journal of Pharmaceutical Sciences* **2023**, *112* (4), 1020–1031. https://doi.org/10.1016/j.xphs.2022.11.014.
(56) Bouarroudj, T.; Aoudjit, L.; Djahida, L.; Zaidi, B.; Ouraghi, M.; Zioui, D.; Mahidine, S.; Shekhar, C.; Bachari, K. Photodegradation of Tartrazine Dye Favored by Natural Sunlight on Pure and (Ce, Ag) Co-Doped ZnO Catalysts. *Water Sci Technol* **2021**, *83* (9), 2118–2134. https://doi.org/10.2166/wst.2021.106.

(57) Jackulin, F.; Senthil Kumar, P.; Boobalan, C.; Rangasamy, G. Mechanism of Sulfate Radical Formation on Activation of Persulfate Using Doped Metal Oxide and Its Role in Degradation of Tartrazine Dye in an Aqueous Solution. *Langmuir* **2024**, *40* (41), 21629–21643. https://doi.org/10.1021/acs.langmuir.4c02692.
(58) Abasalizadeh, F.; Moghaddam, S. V.; Alizadeh, E.; akbari, E.; Kashani, E.; Fazljou, S. M. B.; Torbati, M.; Akbarzadeh, A. Alginate-Based Hydrogels as Drug Delivery Vehicles in Cancer Treatment and Their Applications in Wound Dressing and 3D Bioprinting. *Journal of Biological Engineering* **2020**, *14* (1), 8. https://doi.org/10.1186/s13036-020-0227-7.
(59) Jahani Kadousaraei, M.; Yamada, S.; Aydin, M. S.; Rashad, A.; Cabeza, N. M.; Mohamed-Ahmed, S.; Gjerde, C. G.; Malkoch, M.; Mustafa, K. Bioprinting of Mesenchymal Stem Cells in Low Concentration Gelatin Methacryloyl/Alginate Blends without Ionic Crosslinking of Alginate. *Sci Rep* **2025**, *15* (1), 6609. https://doi.org/10.1038/s41598-025-90389-2.
(60) Wolfgang, M.; Peter, A.; Wahl, P.; Markl, D.; Zeitler, J. A.; Khinast, J. G. At-Line Validation of Optical Coherence Tomography as in-Line/at-Line Coating Thickness Measurement Method. *International Journal of Pharmaceutics* **2019**, *572*, 118766. https://doi.org/10.1016/j.ijpharm.2019.118766.
(61) Moser, N. H.; Landauer, A. K.; Kafka, O. L. IMPPY3D: Image Processing in Python for 3D Image Stacks. *J Open Source Softw* **2025**, *10* (108), 10.21105/joss.07405. https://doi.org/10.21105/joss.07405.
(62) Fischler, M. A.; Bolles, R. C. Random Sample Consensus: A Paradigm for Model Fitting with Applications to Image Analysis and Automated Cartography. *Commun. ACM* **1981**, *24* (6), 381–395. https://doi.org/10.1145/358669.358692.